Plasma Processes and Polymers

PLASMA PROCESSES AND POLYMERS

RESEARCH ARTICLE

Underwater Plasma-Driven Decomposition of Tetramethylammonium Hydroxide (TMAH) Under Different Applied Field Strengths

Ki-Taik Lee[1,2] | Hana Lim[1] | Sung Cheol Park[1,3] | Jin-Young Bae[2] | Sung-Min Kim[1]

[1]Industrial Components R&D Department, Korea Institute of Industrial Technology (KITECH), Incheon, Republic of Korea | [2]Department of Polymer Science and Engineering, Sungkyunkwan University, Suwon, Republic of Korea | [3]Department of Materials Science and Engineering, Inha University, Incheon, Republic of Korea

Correspondence: Sung-Min Kim (sungminkim@kitech.re.kr)

Received: 12 September 2025 | **Revised:** 5 November 2025 | **Accepted:** 11 November 2025

Keywords: hydroxyl radicals | OES | TMAH decomposition | underwater plasma | wastewater treatment

ABSTRACT

Tetramethylammonium hydroxide (TMAH), a toxic and persistent compound widely used in semiconductor manufacturing, was degraded using underwater plasma at applied fields ranging from 0.8 to 10 $kV\,mm^{-1}$. Optical emission spectroscopy revealed OH(A–X), Hβ, and O I features, with Stark broadening of Hβ indicating electron densities between 5.0×10^{24} and $11.8 \times 10^{24}\,m^{-3}$, characteristic of high-field discharge. Spectral analysis showed a field-dependent shift from OH-dominated to O-dominated chemistry. Total organic carbon (TOC) removal followed pseudo-first-order kinetics, with rate constants increasing from 3.6×10^{-3} to $7.7 \times 10^{-3}\,min^{-1}$ but plateauing above 4.8 $kV\,mm^{-1}$. Ion chromatography detected NH_4^+ and NO_3^- accumulation, suggesting that oxidative flux was partially diverted toward nitrogen conversion, thereby competing with carbon mineralization.

1 | Introduction

Tetramethylammonium hydroxide (TMAH) is a quaternary ammonium compound extensively used in the semiconductor industry, particularly as an anisotropic silicon etchant and a photoresist developer in photolithography processes [1, 2]. Its high selectivity toward silicon and compatibility with complementary metal–oxide–semiconductor (CMOS) fabrication steps make TMAH a preferred substitute for hazardous etchants like potassium hydroxide [3]. However, the increasing application of TMAH has led to its accumulation in industrial wastewater, raising significant environmental and occupational health concerns due to its acute toxicity and resistance to biodegradation [4, 5].

Various methods have been investigated to eliminate TMAH from wastewater, including biological processes [6, 7], adsorption [8, 9], and advanced oxidation processes (AOPs) [4, 10, 11]. However, these methods confront important drawbacks. Biological processes are largely ineffective due to the recalcitrance of TMAH to microbial attack [12]. Adsorption techniques only shift the contaminant to another phase, demanding subsequent treatment [13]. Conventional AOPs enable partial degradation but typically depend on external oxidants and may introduce secondary pollutants [4, 14]. These constraints point to an urgent need for novel, high-performance, and environmentally benign approaches to address TMAH contamination.

Underwater plasma has recently emerged as a promising advanced treatment technology. Plasma-based processes are regarded as a subclass of AOPs in which electrical energy, rather than chemical oxidants, drives the formation of reactive species. In such systems, the plasma discharge acts as the primary energy source that activates water molecules, producing hydroxyl radicals, atomic oxygen, solvated electrons, and UV photons that

collectively promote oxidation. This energy-driven oxidation mechanism enables pollutant degradation without the addition of reagents, distinguishing plasma AOPs from conventional UV/H_2O_2, Fenton, or persulfate systems [15, 16]. When a high-voltage discharge is generated directly in water, energetic electrons, radicals (·OH, O·, H·), solvated electrons, and ultraviolet photons are simultaneously produced [17–21]. These reactive species drive non-selective oxidation of persistent organic pollutants without the need for chemical additives. Compared with conventional AOPs, plasma-based processes operate under ambient conditions, minimize secondary waste, and can be tuned through discharge parameters [22]. Previous studies have demonstrated the effectiveness of underwater plasma in decomposing dyes [23, 24], perfluorinated compounds [25, 26], and other refractory organics [27], but its application to TMAH remains scarcely explored.

To establish underwater plasma as a viable option for treating TMAH, a fundamental understanding of both plasma characteristics and degradation pathways is required. In particular, the optical emission spectrum (OES) provides valuable information about excited species and electron density, which are directly linked to plasma reactivity [28–30]. Moreover, quantifying degradation kinetics and identifying inorganic nitrogen by-products (e.g., NO_3^-, NH_4^+) are essential to elucidate the decomposition mechanism and assess potential secondary pollution.

In this study, we investigate the underwater plasma-driven decomposition of TMAH under different applied electric field strengths. Broadband OES was employed to monitor reactive species, while Voigt profile fitting of the Hβ line enabled estimation of electron densities based on Stark broadening. The time-dependent removal of total organic carbon (TOC) was analyzed to evaluate kinetic behavior, and ion chromatography (IC) was used to identify nitrogen-containing by-products. By correlating plasma diagnostics with degradation performance, we clarify the role of discharge intensity in TMAH decomposition and demonstrate a field-dependent transition from OH- to O-dominated oxidation. This mechanistic insight provides a foundation for future optimization of additive-free plasma-based treatment processes for semiconductor wastewater.

2 | Experimental Section

2.1 | Underwater Plasma Discharge

Tungsten rods (W, 99.995%, 1 mm diameter, Alfa Aesar) were used as electrode stock materials. The discharge reactor was fabricated from polytetrafluoroethylene (PTFE) with a total working volume of 200 cm^3 (Figure 1a). Two tungsten electrodes (1.0 mm diameter) were installed horizontally, facing each other and immersed several millimeters below the liquid surface [28, 31]. The interelectrode gap was precisely adjusted between 0.3 and 2.0 mm. TMAH pentahydrate ($(CH_3)_4N(OH)\cdot 5H_2O$, ≥ 97%, Sigma-Aldrich) was used to prepare aqueous solutions with an initial concentration of 1.0×10^{-2} kg m^{-3}, employing deionized (DI) water (18.2 MΩ·cm) from a Millipore Direct Q-3 system. A bipolar pulsed power supply (KURITA Seisakusho Co. Ltd) was used to generate the underwater discharge, delivering 1.6–3.0 kV at 25 kHz with a pulse width of 2.5 μs. Depending on the applied voltage (V) and electrode gap (d), the apparent electric field ($E_{app} = V/d$) ranged from approximately 0.8 to 10 kV mm^{-1}. We note that E_{app} is an estimate, the local microfield in the discharge channel can exceed V/d. Discharge experiments were conducted for 60 min while a recirculating chiller maintained the solution temperature at 297.15 ± 1 K, effectively dissipating discharge-generated heat and preventing secondary thermal effects so that the observed degradation reflects plasma-chemical rather than thermal processes. A representative photograph of the plasma discharge is shown in Figure 1b. All experiments were performed in triplicate ($n = 3$).

Optical emission spectroscopy (OES) was carried out in situ using a fiber-coupled spectrometer (Ocean Optics, USB4000). The optical probe (UV–VIS fiber with a 600 μm core) was positioned to collect light through a quartz viewport at the discharge height. Spectra were collected via a laptop and analyzed for the OH (A–X, 306–310 nm), Hβ (483–500 nm), and O I (774–782 nm) lines after linear baseline subtraction and dark correction. The Hβ line was fitted using a Voigt profile. The Gaussian full width at half maximum (FWHM) reflects both the instrumental resolution, approximately 0.8 nm, and Doppler

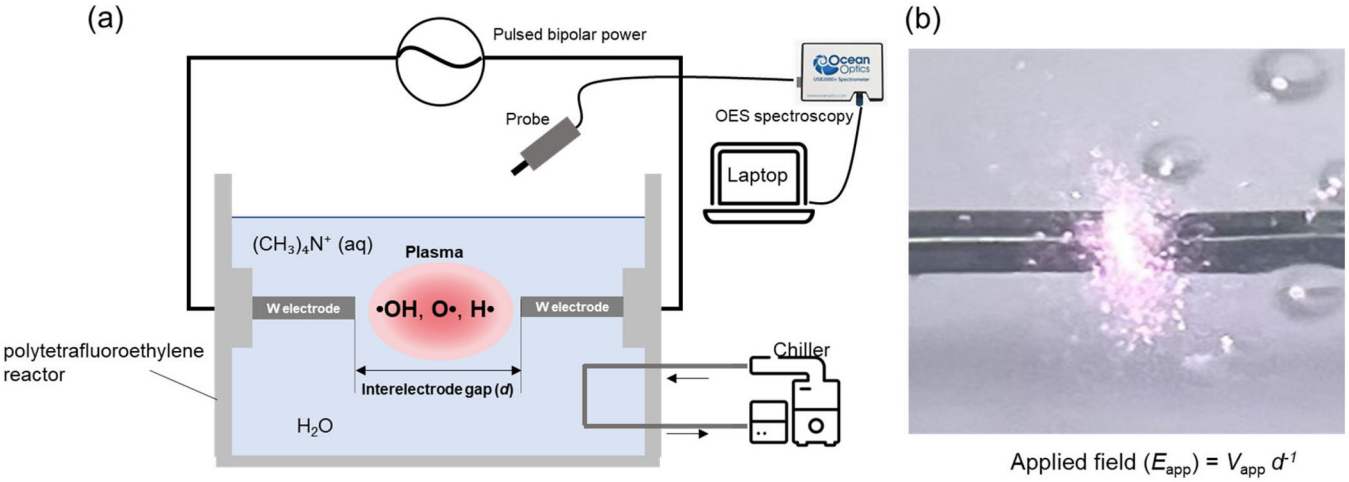

FIGURE 1 | (a) Schematic illustration of the underwater plasma reactor for TMAH degradation. (b) Submerged-plasma photograph during operation.

broadening. The Lorentzian component of the FWHM, denoted as ΔλL, is interpreted as arising from Stark broadening. The instrumental function (~0.8 nm) was measured with a low-pressure calibration lamp and deconvolved before fitting. Electron density (n_e) was obtained from $\Delta\lambda_L$ using tabulated Hβ Stark widths [32]. Following the common semi-empirical scaling.

$$n_e(\mathrm{cm}^{-3}) = 10^{16}(\Delta\lambda_L/0.94666)^{1.49},\ n_e(\mathrm{m}^{-3}) = 10^6 \times n_e(\mathrm{cm}^{-3}) \quad (1)$$

Uncertainty from the fit (SE of $\Delta\lambda_L$) and from gas-temperature assumptions (±100 K for Doppler) was propagated to the n_e error bars. Van der Waals and ion broadening were evaluated and found to be negligible under our conditions.

2.2 | Degradation Analysis

The degradation of TMAH was monitored by measuring TOC using a TOC analyzer (multi N/C 2100 S, Analytik Jena) based on high-temperature catalytic combustion. Samples (5–10 cm^3) were withdrawn at designated intervals, immediately quenched by rapid cooling, filtered through 0.22 μm PTFE membranes, and analyzed within 24 h. A discharge-off control (stirring only) was included and showed no measurable TOC change over 60 min. TOC removal efficiencies were used to evaluate the decomposition of TMAH, and pseudo-first-order kinetics were applied to derive the apparent rate constants [33].

$$\ln(c/c_0) = -kt \quad (2)$$

where c_0 and c represent the initial and time-dependent TOC concentrations (mg m^{-3}), respectively, t is the discharge time (min), and k is the apparent rate constant (min^{-1}). Kinetic fits were performed on the 0–60 min window. k values are reported with 95% confidence intervals.

The mean relative deviation (*MRD*) was calculated to assess the goodness of fit according to Equation (3) [34]:

$$MRD = \frac{1}{n}\sum_{i=1}^{n}\frac{|c_{\mathrm{exp},i} - c_{cal,i}|}{c_{\mathrm{exp},i}} \times 100 \quad (3)$$

where $c_{\mathrm{exp,i}}$ and $c_{\mathrm{cal,i}}$ represent the experimentally measured and model-calculated TOC concentrations at each sampling point, respectively, and n is the number of data points.

Inorganic nitrogen species generated during TMAH degradation were analyzed by ion chromatography (IC, Metrohm 850 Professional IC) equipped with a conductivity detector. Anion species (NO_3^-) were quantified using an anion separation column (Metrohm Metrosep A Supp 5, 250/4.0 mm) with carbonate/bicarbonate eluent and chemical suppression. Ammonium (NH_4^+) was determined either by cation IC (Metrosep C 4, 250/4.0 mm) or cross-validated by the indophenol blue colorimetric method. Before analysis, samples were filtered through 0.22 μm membranes and diluted with DI water as needed to fall within the calibration range. All TOC/IC results are reported as mean ± SD for $n = 3$ independent runs. For comparability with carbon removal, NO_3^- and NH_4^+ are additionally expressed on a mol-N basis as c/c_0.

3 | Results and Discussion

3.1 | Field-Dependent Plasma Chemistry

To probe the chemical environment of the submerged discharge, we employed in situ OES. The broadband spectra and representative diagnostic windows are shown in Figure 2. Under progressively stronger applied fields in 1.0×10^{-2} kg m^{-3} TMAH solution, three spectral signatures dominate the chemistry, namely the OH (A–X, 0–0) band at 306–312 nm, the Hβ line near 486.1 nm, and the O I triplet region around 777 nm. Their concurrent appearance reflects the multifaceted chemistry of the plasma–liquid interface. Hydroxyl radicals are generated through electron-impact dissociation and excitation of H_2O, while excited hydrogen species arise from fragmentation and subsequent recombination pathways [35, 36]. Atomic oxygen is produced via electron-induced cleavage of H_2O or oxygen-bearing intermediates. These assignments are consistent with canonical plasma–water reactions, which could be expressed as follows:

$$e + H_2O \rightarrow OH\cdot + H\cdot + e \quad (3')$$

$$e + H_2O \rightarrow O\cdot + H_2 + e \quad (4)$$

with subsequent electronic relaxation processes yielding the observed emission bands.

Magnified views of the diagnostic windows (Figures 2b–d) reveal that all three emissions intensify with increasing applied field. OH (A–X) and O I signals exhibit pronounced growth, consistent with enhanced production of hydroxyl radicals and atomic oxygen at higher field strength. Hβ emission also increases, reflecting stronger hydrogen excitation as water fragmentation becomes more pronounced. In addition to intensity changes, the emission lines broaden progressively with applied field, indicating higher electron densities under high-field discharge conditions. These observations demonstrate that the plasma generates a chemically rich environment whose composition and strength are strongly field-dependent. A more detailed quantitative comparison of relative emission yields is presented later (Figure 4). It is also noteworthy that nitrogen-related emission bands (e.g., NO, NH) were absent, plausibly due to the low TMAH concentration (1.0×10^{-2} kg m^{-3}), where nitrogen fragments are only present in trace amounts relative to dominant water-derived species. Consequently, the emission spectra emphasize that the submerged plasma is governed primarily by water dissociation chemistry, yielding a rich oxidative environment that drives the subsequent degradation of TMAH.

Figure 3a presents normalized Hβ emission spectra fitted with Voigt profiles under applied fields ranging from 0.8 to 10 kV mm^{-1}. Spectra were normalized to their peak intensities to reveal line-shape variations rather than absolute intensity changes. As the field increases, the Hβ line exhibits clear

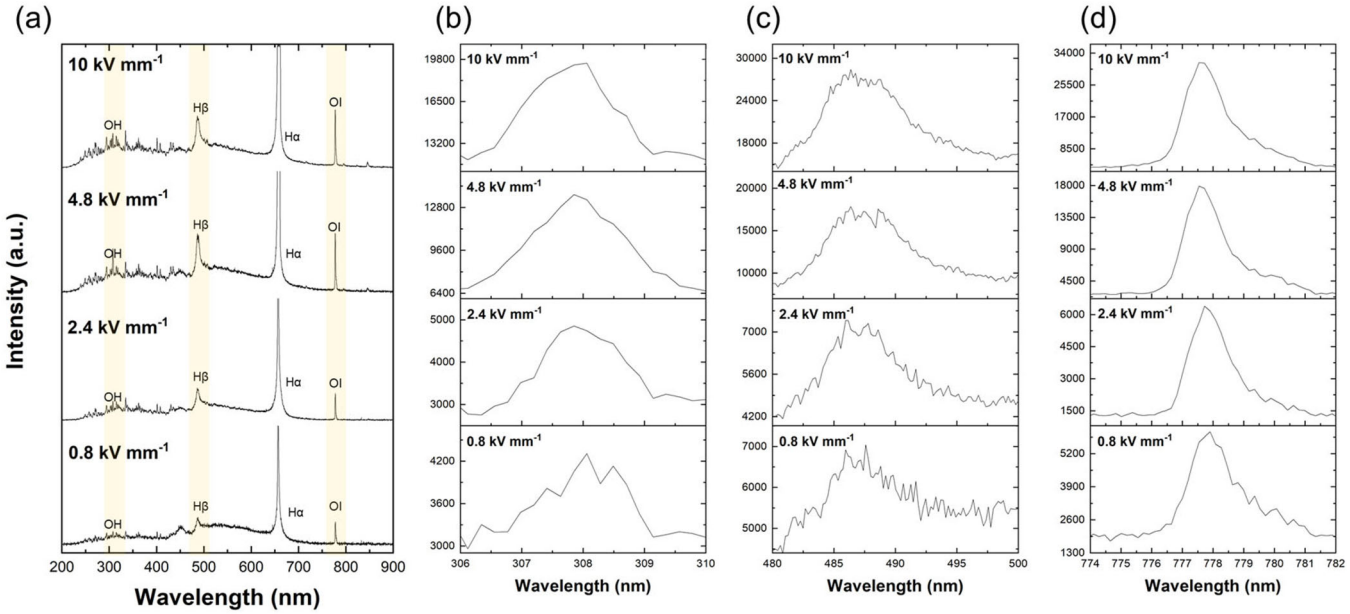

FIGURE 2 | (a) Broadband emission spectra at different applied electric fields (0.8–10 kV mm^{-1}), with highlighted OH (A–X), Hβ, and O I regions. (b–d) Zoomed windows for OH (A–X), Hβ, and O I (777 nm), respectively.

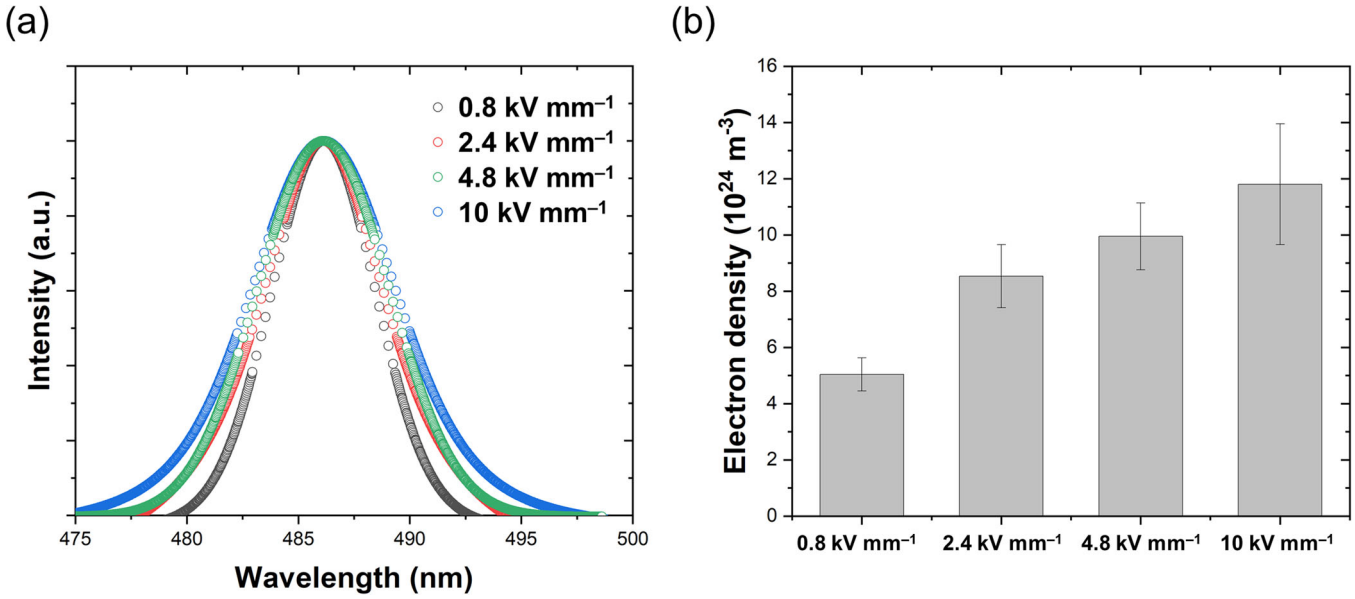

FIGURE 3 | (a) Normalized Hβ emission spectra fitted with Voigt functions under different applied electric fields (0.8–10 kV mm^{-1}). The broadening of the Hβ line increases with the applied field strength. (b) Electron density estimated from Stark broadening of the Lorentzian component of Hβ as a function of electric field, indicating values in the arc discharge regime.

broadening, consistent with enhanced Stark effects at higher plasma power densities. The Voigt function effectively captures the line profile, enabling separation of Gaussian components (instrumental ~0.8 nm and Doppler broadening) from the Lorentzian contribution associated with electron–impact interactions. n_e was estimated from the Lorentzian FWHM using Eq. (1) in the Experimental section. Figure 3b summarizes the results, showing a monotonic increase in n_e from 5.04×10^{24} m^{-3} at 0.8 kV mm^{-1} to 11.8×10^{24} m^{-3} at 10 kV mm^{-1}. These values place the discharge firmly within the high-field plasma regime, with electron densities two to three orders of magnitude higher than those typical of glow discharges. The obtained electron densities (10^{24}–10^{25} m^{-3}) are consistent with ranges reported for arc discharges in the literature [37], and significantly exceed those of conventional glow discharges (10^{20}–10^{22} m^{-3}). The increase in electron density with field supports the interpretation that the plasma evolves from a relatively diffuse discharge at lower fields toward a more filamentary state at higher fields. Together, Figures 3a,b demonstrate that Stark broadening of Hβ provides a quantitative probe of electron density, directly linking discharge field strength to plasma behavior. The obtained electron densities (5.0×10^{24}–1.2×10^{25} m^{-3}) are in excellent agreement with values reported for underwater arc and streamer discharges (10^{24}–10^{25} m^{-3}) in previous studies [37]. This confirms that the discharge progressively evolves from a diffuse streamer at low

field to an arc-like regime at higher intensity, consistent with the enhanced emission and power density observed.

Although no nitrogen-related emission lines were observed in the optical spectra, this does not exclude nitrogen chemistry in the plasma–liquid system. The excitation cross-sections of N_2 and NO_x species are extremely low under aqueous conditions, and their excited states are efficiently quenched by water vapor and oxygen near the interface. As shown later by IC, nitrogen-containing products (NH_4^+, NO_3^-) are instead formed in the liquid phase through plasma-induced redox reactions involving solvated electrons, •H, and NO_2/NO intermediates.

To further quantify emission characteristics, the integrated areas of OH, Hβ, and O I bands were calculated after baseline subtraction and are summarized in Supporting Information S1: Table 1. The absolute intensities of OH, Hβ, and O I emissions increase with the applied electric field. However, this trend alone does not clarify the relative efficiency of radical generation. To enable more meaningful comparisons across discharge conditions, integrated intensity ratios such as I(OH)/I(Hβ) and I(O)/I(Hβ) were calculated. By normalizing against hydrogen emission, these ratios provide a consistent basis for evaluating radical production. Figure 4 presents the area-integrated emission intensity ratios I(OH)/I(Hβ) and I(O)/I(Hβ) as functions of the applied field strength. The I(OH)/I(Hβ) ratio increases steadily from 0.8 to 4.8 kV mm^{-1}, indicating progressively enhanced OH radical production relative to hydrogen excitation. At 10 kV mm^{-1}, however, the ratio declines. This suggests that OH (A–X) emission does not scale proportionally with discharge power. Several factors may contribute to this rollover. Collisional quenching of OH ($A^2\Sigma^+$) becomes significant at elevated gas temperatures near arc filaments [37]. Recombination reactions such as $OH + H \rightarrow H_2O$ may also intensify, reducing OH availability [38]. In addition, reactive nitrogen and oxygen intermediates in air-saturated water can scavenge OH radicals, forming NO_x species and diverting the oxidative pathway [39]. In contrast, the I(O)/I(Hβ) ratio rises continuously across the entire field range, with a sharp increase beyond approximately 4.8 kV mm^{-1}. This trend reflects a shift toward oxygen-dominated chemistry under high-field discharge conditions. Elevated electron densities, as shown in Figure 3, support more efficient electron-impact dissociation of H_2O, yielding atomic oxygen. The persistence of O emission at 10 kV mm^{-1} indicates that O-based oxidation mechanisms remain active even at the highest discharge intensity. These observations reveal a transition in the plasma's oxidative behavior. OH radicals dominate at moderate fields but are suppressed at peak power, while atomic oxygen production continues to accelerate. Normalized emission ratios offer a more reliable diagnostic than absolute intensities, linking plasma conditions to chemical reactivity. In the context of TMAH decomposition, the data imply that O atoms and their secondary products become increasingly central under arc-like regimes, whereas OH radicals play a more prominent role at lower field strengths.

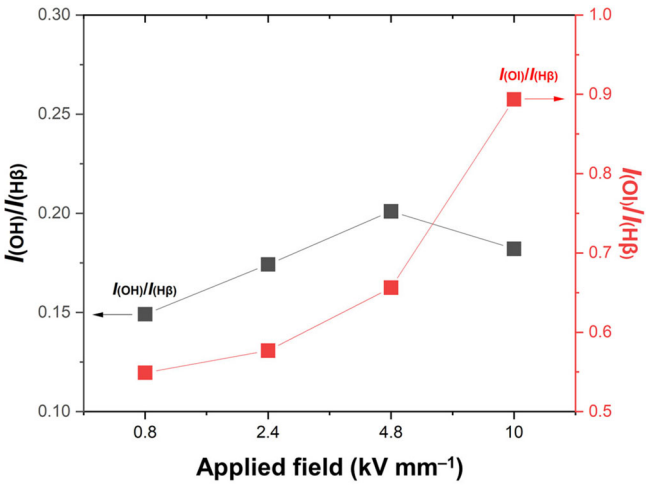

FIGURE 4 | Integrated emission intensity ratios, I(OH)/I(Hβ) and I(O)/I(Hβ), as a function of applied electric field strength. The ratios were derived from area-integrated spectral bands and provide a relative measure of hydroxyl radical and atomic oxygen generation normalized to hydrogen emission.

3.2 | Degradation Performance

The degradation of TMAH via underwater plasma was evaluated by monitoring TOC over time. As shown in Figure 5a, normalized TOC concentrations (c/c_0) decreased progressively with treatment duration across all tested electric field strengths (0.8–10 kV mm^{-1}). The TOC removal efficiency was strongly field-dependent, with only ~20% TOC reduction at 0.8 kV mm^{-1} and over 37% at 10 kV mm^{-1} after 60 min (Table 1). These results correlate with OES (Figures 2–4), which revealed increased electron densities and enhanced generation of oxidative species at higher discharge intensities. Kinetic analysis using a pseudo-first-order model ($\ln(c/c_0) = -kt$) yielded linear fits (Figure 5b), confirming the model's applicability. The apparent rate constants (k), summarized in Table 1, increased systematically with field strength, from 3.58×10^{-3} min^{-1} at 0.8 kV mm^{-1} to 7.65×10^{-3} min^{-1} at 10 kV mm^{-1}. This trend demonstrates the role of discharge intensity in accelerating radical-driven degradation. The enhanced TOC removal is consistent with plasma diagnostics. n_e increased by approximately 2.3 times across the tested field range (Figure 3 and Table 1), promoting electron-impact dissociation of water and generation of OH and O species. Emission ratio analysis (Figure 4) indicated a shift from OH-dominated oxidation at moderate fields to O-dominated pathways under applied field strength of 10 kV mm^{-1} [40]. Importantly, the apparent rate constant plateaued between 4.8 and 10 kV mm^{-1}, suggesting that further increases in discharge intensity did not proportionally enhance TOC degradation. This observation implies that, beyond a certain threshold, radical-driven oxidation pathways become saturated or diverted. The pseudo-first-order fittings exhibited excellent linearity with $R^2 > 0.97$ and *MRD* below 1.5%, confirming the robustness of the kinetic model. The apparent rate constants obtained in this study ($3.58–7.65 \times 10^{-3}$ min^{-1}) are comparable to or higher than those reported for other AOP-based TMAH degradation systems. For instance, Kim et al. [41] achieved 7.8×10^{-3} min^{-1} with 65% TOC removal using a nano-ozone/H_2O_2 process, while Jung et al. [10] reported 1.8×10^{-2} min^{-1} in an O_3/peroxymonosulfate system (Supporting Information S1: Table 2). In contrast, cold plasma + periodate oxidation [4] and Ag/TiO_2

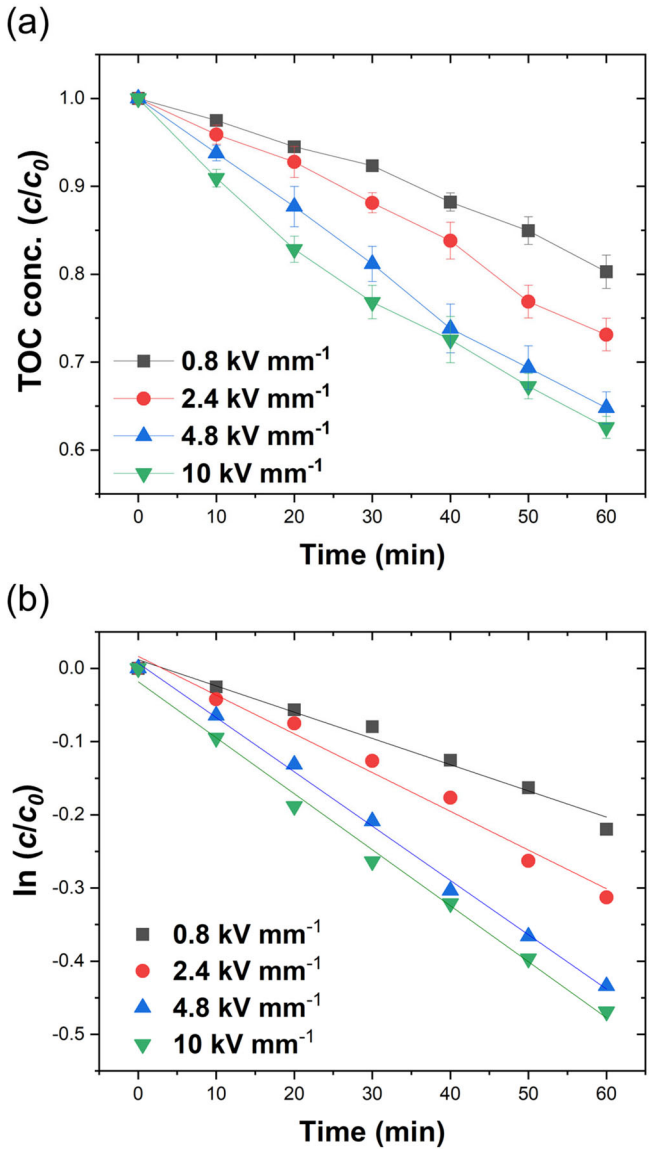

FIGURE 5 | Time-dependent TOC degradation of TMAH: (a) normalized TOC concentration (c/c_0) versus discharge time, and (b) pseudo-first-order fitting of $\ln(c/c_0)$ for kinetic analysis.

photoelectrocatalysis [42] exhibited k values in the range of 10^{-3}–10^{-2} min^{-1} but required external oxidants or catalysts. Despite moderate TOC removal (37%), the underwater plasma process achieved comparable kinetic performance without additive chemicals, highlighting its environmental and operational advantages. To elucidate the fate of nitrogen under these conditions, IC was employed to quantify NH_4^+ and NO_3^- as major by-products, providing insight into the redistribution of reactive nitrogen species and confirming that incomplete TOC degradation is accompanied by parallel conversion of nitrogen into stable inorganic forms.

Figure 6 presents the time-dependent accumulation of NH_4^+–N and NO_3^-–N, each normalized to the initial nitrogen content. Both species increased progressively throughout plasma treatment, with their concentrations strongly influenced by the applied electric field strength. After 60 min, NH_4^+–N reached 0.069, 0.092, 0.151, and 0.176 (c/c_0) for applied fields of 0.8, 2.4, 4.8, and 10 kV mm^{-1}, respectively. NO_3^-–N followed a similar trend, rising to 0.071, 0.099, 0.189, and 0.221 under the same conditions. These results indicate that higher discharge intensities facilitate not only TOC removal but also the conversion of nitrogen into stable ionic forms. The simultaneous formation of NH_4^+ and NO_3^- reflects the operation of distinct plasma-driven nitrogen pathways. NH_4^+ is produced through reductive fragmentation of the tetramethylammonium cation, followed by protonation in solution [43, 44]. This mechanism is consistent with the known vulnerability of quaternary ammonium groups to electron-induced cleavage [45]. In contrast, NO_3^- formation proceeds via oxidative routes involving reactive oxygen and nitrogen intermediates [46]. Electron-impact dissociation of dissolved N_2 and O_2 generates excited nitrogen species (N_2*) and atomic oxygen (O·), which recombine to form NO and NO_2 [45, 47]. While NO and NO_2 band emissions were not resolved in the OES, the steady accumulation of NO_3^- (IC) indirectly evidences nitrogen–oxygen intermediates, indicating diversion of oxidative flux toward NO_x chemistry at high fields. This indicates that nitrogen–oxygen intermediates indeed form during the discharge and compete with carbon oxidation by consuming OH radicals, thereby diverting part of the oxidative capacity toward NO_x chemistry. These intermediates are subsequently oxidized to NO_3^- in the aqueous phase. The pronounced increase in NO_3^- concentration between 4.8 and 10 kV mm^{-1} corresponds with the optical emission data shown in Figure 4, which reveal a shift toward oxygen-dominated chemistry under high-field discharge conditions. Taken together, the IC data reveal that incomplete TOC degradation is accompanied by parallel nitrogen conversion, and that the balance between these processes is governed by discharge intensity. At moderate fields (4.8 kV mm^{-1}), OH-mediated carbon oxidation is efficient. At higher fields of 10 kV mm^{-1}, however, O- and NO_x-driven reactions prevail, redirecting reactive flux toward inorganic nitrogen formation. This shift accounts for the saturation in TOC removal despite continued increases in electron density and radical production.

Bulk pH decreased steadily over time, with a sharper decline observed at higher applied electric fields, as shown in Figure 7. In contrast, the discharge-off control remained stable around 9.7–9.8. After 60 min of treatment, the pH values were 8.15 ± 0.12 at 0.8 kV mm^{-1}, 8.01 ± 0.10 at 2.4 kV mm^{-1}, 7.63 ± 0.02 at 4.8 kV mm^{-1}, and 7.29 ± 0.04 at 10 kV mm^{-1}. The pH change followed a biphasic pattern. During the first 10–20 min, a rapid drop occurred due to the dissolution of air-derived NO and NO_2 along with CO_2. This was followed by a plateau phase, where the rate of acidification became limited by mass transfer. The resulting moderate acidification, which scaled with the applied field, created an environment where NO_x species actively scavenged OH radicals. This condition is consistent with the observed suppression of I(OH)/I(Hβ) growth at 10 kV mm^{-1}. It also helps explain the plateau in TOC removal kinetics between 4.8 and 10 kV mm^{-1}, despite the presence of a more intense discharge regime. The observed acidification originates from the dissolution of air-derived NO and NO_2 together with CO_2, forming HNO_2, HNO_3, and H_2CO_3 [48]. As the pH decreases, protonation equilibria shift, and secondary reactions become increasingly significant. Under acidic conditions, reactive nitrogen species such as NO_2•, NO•, and peroxynitrite ($ONOO^-$/ONOOH) are formed more readily. These species effectively scavenge •OH radicals, reducing

TABLE 1 | Summary of TOC decomposition efficiency and apparent first-order rate constant (k) for TMAH degradation under underwater plasma treatment.

E_{app} [kV mm^{-1}]	n_e [10^{24} m^{-3}]	TOC removal after 60 min [%]	Apparent rate constant, $-k$ [$\times 10^{-3}$ min^{-1}]	R^2	*MRD* [%]
0.8	5.04	19.7	3.58	0.980	0.85
2.4	8.53	26.9	5.29	0.982	1.39
4.8	9.95	35.2	7.42	0.997	0.67
10	11.8	37.4	7.65	0.994	0.96

Note: Data are shown as a function of applied electric field, along with corresponding electron densities (n_e) after 60 min treatment of 1.0×10^{-2} kg m^{-3} TMAH solution.

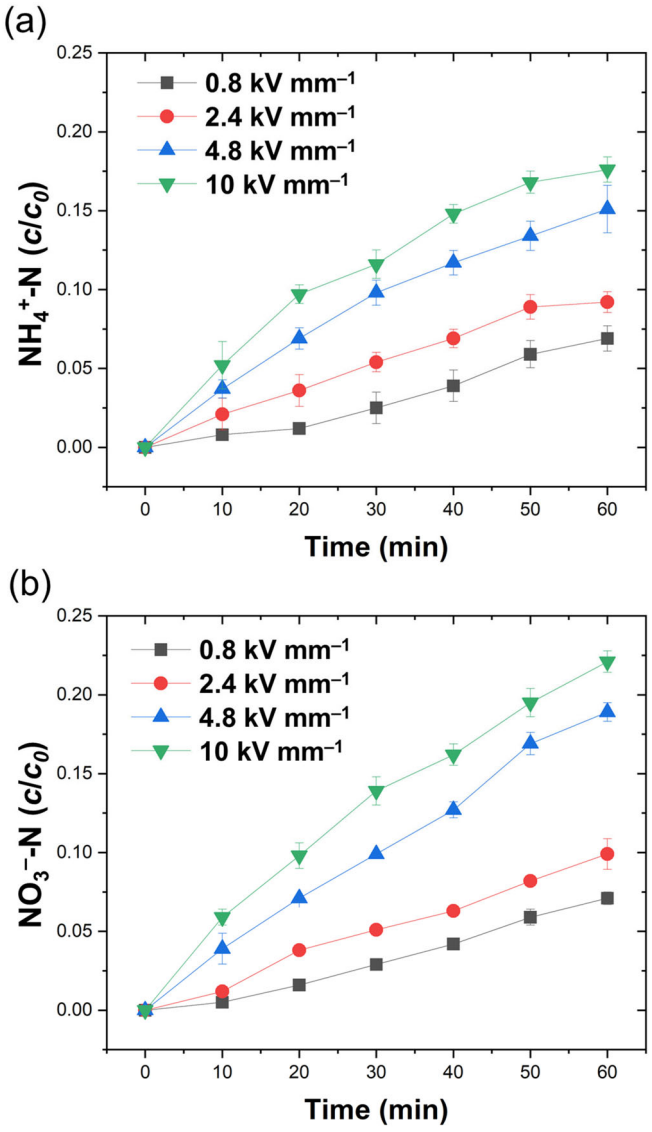

FIGURE 6 | Formation of inorganic nitrogen species (NH_4^+ and NO_3^-) during TMAH degradation as determined by ion chromatography. (a) NH_4^+–N evolution and (b) NO_3^-–N evolution as a function of treatment time at various applied electric fields.

their availability and thereby suppressing further oxidation of TMAH [49]. This shift in radical dynamics suggests that plasma-induced acidification modulates the balance between •OH-driven and O/NO_x-driven oxidation pathways, consistent with the emission ratio transitions observed in Figures 4 and 7.

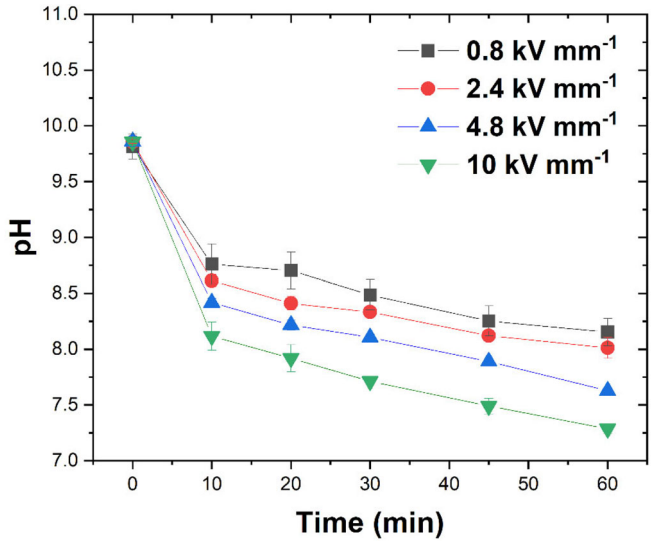

FIGURE 7 | Bulk pH as a function of discharge time under different applied fields.

4 | Conclusion

Underwater plasma effectively decomposed TMAH, with degradation strongly governed by the applied electric field. OES analysis showed that higher fields increased electron density and promoted radical generation, while emission ratios revealed a transition from OH- to O-dominated oxidation. TOC removal followed pseudo-first-order kinetics, but the rate constant plateaued between 4.8 and 10 kV mm^{-1}, suggesting that additional energy input no longer enhanced carbon mineralization. Concurrent nitrogen conversion to NH_4^+ and NO_3^- indicated competition between carbon and nitrogen oxidation under high-field conditions. These results establish discharge intensity as a critical parameter for optimizing plasma-driven wastewater treatment. From a practical perspective, the process operates without external oxidants, features a simple modular design, and holds promise for scalable, cost-effective treatment of semiconductor effluents.

Acknowledgments

This study was supported by the project (UR250012 and IZ250015), as part of the "Incheon-Specialized Semiconductor Industry Ecosystem Development Initiative."

Conflicts of Interest

The authors declare no conflicts of interest.

Data Availability Statement

The data that support the findings of this study are available from the corresponding author upon reasonable request.

References

1. A. H. Romang and J. J. Watkins, "Supercritical Fluids for the Fabrication of Semiconductor Devices: Emerging or Missed Opportunities?," *Chemical Reviews* 110 (2010): 459–478.

2. D. P. Sanders, "Advances in Patterning Materials for 193 Nm Immersion Lithography," *Chemical Reviews* 110 (2010): 321–360.

3. O. Tabata, R. Asahi, H. Funabashi, K. Shimaoka, and S. Sugiyama, "Anisotropic Etching of Silicon in TMAH Solutions," *Sensors and Actuators, A: Physical* 34 (1992): 51–57.

4. H. J. Kim, H. Kim, U. Lee, H. S. Oh, H. W. Kim, and J. Lee, "Removal of Tetramethylammonium Hydroxide (TMAH) by Cold Plasma Treatment Combined with Periodate Oxidation: Degradation, Kinetics, and Toxicity Study," *Chemosphere* 362 (2024): 142704.

5. I. C. Mori, C. R. Arias-Barreiro, A. Koutsaftis, et al., "Toxicity of Tetramethylammonium Hydroxide to Aquatic Organisms and its Synergistic Action with Potassium Iodide," *Chemosphere* 120 (2015): 299–304.

6. T. H. Hu, L. M. Whang, P. W. G. Liu, et al., "Biological Treatment of TMAH (Tetra-Methyl Ammonium Hydroxide) in a Full-Scale TFT-LCD Wastewater Treatment Plant," *Bioresource Technology* 113 (2012): 303–310.

7. B. Liu, K. Yoshinaga, J. H. Wu, et al., "Kinetic Analysis of Biological Degradation for Tetramethylammonium Hydroxide (TMAH) in the Anaerobic Activated Sludge System at Ambient Temperature," *Biochemical Engineering Journal* 114 (2016): 42–49.

8. S. Chang, K. Y. A. Lin, and C. Lu, "Efficient Adsorptive Removal of Tetramethylammonium Hydroxide (TMAH) from Water Using Graphene Oxide," *Separation and Purification Technology* 133 (2014): 99–107.

9. B. P. Kelleher, A. M. Doyle, T. F. O'Dwyer, and B. K. Hodnett, "Preparation and Use of a Mesoporous Silicate Material for the Removal of Tetramethyl Ammonium Hydroxide (TMAH) from Aqueous Solution," *Journal of Chemical Technology & Biotechnology* 76 (2001): 1216–1222.

10. H. Jung, D. Jang, J. Jung, C. Lee, and A. Jang, "Application of an Ozone-Activated Peroxymonosulfate Process to Effectively Degrade Tetramethylammonium Hydroxide (TMAH) in Semiconductor Wastewater," *Journal of Water Process Engineering* 67 (2024): 106141.

11. C. W. Wang and C. Liang, "Oxidative Degradation of TMAH Solution with UV Persulfate Activation," *Chemical Engineering Journal* 254 (2014): 472–478.

12. G. Moretti, F. Matteucci, M. Saraullo, F. Vegliò, and M. Del Gallo, "Selection of a Very Active Microbial Community for the Coupled Treatment of Tetramethylammonium Hydroxide and Photoresist in Aqueous Solutions," *International Journal of Environmental Research and Public Health* 15 (2018): 41.

13. Z. W. Zhang, Y. H. Wu, Z. Y. Xiao, et al., "Treatment Technologies and Mechanisms for Tetramethylammonium Hydroxide (TMAH) Wastewater from Micro-Electronic Industry: A Review," *Resources, Conservation and Recycling* 194 (2023): 106999.

14. J. Huang, K. S. Wang, and C. Liang, "Oxidative Degradation of Tetramethylammonium Hydroxide (TMAH) by UV/Persulfate and Associated Acute Toxicity Assessment," *Journal of Environmental Science and Health, Part A* 52 (2017): 930–937.

15. M. Petrović, M. Kostić, S. Rančev, et al., "Co-Doped ZnO Catalyst for Non-Thermal Atmospheric Pressure Pulsating Corona Plasma Degradation of Reactive Dye," *Materials Chemistry and Physics* 325 (2024): 129733.

16. M. Petrović, S. Rančev, M. Prekajski Đorđević, et al., "Electrochemically Synthesized Molybdenum Oxides for Enhancement of Atmospheric Pressure Non-Thermal Pulsating Corona Plasma Induced Degradation of an Organic Compound," *Chemical Engineering Science* 230 (2021): 116209.

17. P. Bruggeman and C. Leys, "Non-Thermal Plasmas in and in Contact with Liquids," *Journal of Physics D: Applied Physics* 42 (2009): 053001.

18. B. R. Locke, M. Sato, P. Sunka, M. R. Hoffmann, and J. S. Chang, "Electrohydraulic Discharge and Nonthermal Plasma for Water Treatment," *Industrial & Engineering Chemistry Research* 45 (2006): 882–905.

19. Y. K. Heo, S. H. Lee, M. A. Bratescu, S. M. Kim, G. J. Lee, and N. Saito, "Generation of Non-Equilibrium Condition in Solution Plasma Discharge Using Low-Pass Filter Circuit," *Plasma Processes and Polymers* 14 (2017): 1600163.

20. H. Zhu, Y. Luo, D. Liu, S. Zhang, and X. Lu, "Enhancing Mass Transfer of Reactive Oxygen and Nitrogen Species in Plasma-Activated Water: A Molecular Dynamics Study on the Impact of Plasma Electric Fields," *Plasma Processes and Polymers* 22 (2025): 2400214.

21. P. Lu, D. Boehm, P. Bourke, and P. J. Cullen, "Achieving Reactive Species Specificity within Plasma-Activated Water Through Selective Generation Using Air Spark and Glow Discharges," *Plasma Processes and Polymers* 14 (2017): 1600207.

22. N. Morin-Crini, E. Lichtfouse, M. Fourmentin, et al., "Removal of Emerging Contaminants from Wastewater Using Advanced Treatments. A Review," *Environmental Chemistry Letters* 20 (2022): 1333–1375.

23. R. Zhou, T. Zhang, R. Zhou, et al., "Underwater Microplasma Bubbles for Efficient and Simultaneous Degradation of Mixed Dye Pollutants," *Science of the Total Environment* 750 (2021): 142295.

24. A. Khlyustova and N. Sirotkin, "One-Stage Method for Removing Dyes under the Action of Underwater Plasma and Ferrites of Cobalt, Nickel, and Titanium," *Plasma Chemistry and Plasma Processing* 44 (2024): 1797–1810.

25. S. Sun, B. Sun, X. Zhu, Y. Yang, and H. Liu, "Defluorination of Per-Fluorinated Compound (PFC) by Microwave Discharge Plasma in Liquid: A Green and Efficient Water Treatment Technology," *Separation and Purification Technology* 319 (2023): 124071.

26. K. Papalexopoulou, X. Huang, A. Ronen, and C. A. Aggelopoulos, "Reactive Species and Mechanisms of Perfluorooctanoic Acid (PFOA) Degradation in Water by Cold Plasma: The Role of HV Waveform, Reactor Design, Water Matrix and Plasma Gas," *Separation and Purification Technology* 342 (2024): 126955.

27. S. Liu, Y. Kang, and W. Hua, "Efficient Degradation of the Refractory Organic Pollutant by Underwater Bubbling Pulsed Discharge Plasma: Performance, Degradation Pathway, and Toxicity Prediction," *Environmental Science and Pollution Research* 30 (2023): 100596–100612.

28. K. T. Lee, G. B. Seong, B. H. Jeong, and S. M. Kim, "Enhanced Thermal Conductivity via Submerged Plasma-Synthesized Silver Nanostructures," *Materials Letters* 391 (2025): 138518.

29. S. M. Kim and S. Y. Lee, "The Plasma-Induced Formation of Silver Nanocrystals in Aqueous Solution and Their Catalytic Activity for Oxygen Reduction," *Nanotechnology* 29 (2018): 085602.

30. S. M. Kim, Y. G. Jo, M. H. Lee, N. Saito, J. W. Kim, and S. Y. Lee, "The Plasma-Assisted Formation of Ag@Co3O4 Core-Shell Hybrid Nanocrystals for Oxygen Reduction Reaction," *Electrochimica Acta* 233 (2017): 123–133.

31. S. M. Kim, G. S. Kim, and S. Y. Lee, "Effects of PVP and KCl Concentrations on the Synthesis of Gold Nanoparticles Using a Solution Plasma Processing," *Materials Letters* 62 (2008): 4354–4356.

32. M. A. Gigosos, M. Á. González, and V. Cardeñoso, "Computer Simulated Balmer-Alpha, -Beta and -Gamma Stark Line Profiles for

Non-Equilibrium Plasmas Diagnostics," *Spectrochimica Acta, Part B: Atomic Spectroscopy* 58 (2003): 1489–1504.

33. J. Mitrović, M. Radović Vučić, M. Kostić, et al., "Comparative Evaluation of UV-C-Activated Peroxide and Peroxydisulfate for Degradation of a Selected Herbicide," *Separations* 12 (2025): 116.

34. S. M. Najdanović, M. M. Kostić, M. M. Petrović, et al., "Effect of Electrochemical Synthesis Parameters on the Morphology, Crystal and Chemical Structure, and Sorption Efficiency of Basic Bismuth Nitrates," *Molecules* 30 (2024): 1020.

35. S. Mohades, A. M. Lietz, J. Kruszelnicki, and M. J. Kushner, "Helium Plasma Jet Interactions with Water in Well Plates," *Plasma Processes and Polymers* 17 (2020): 1900179.

36. Y. Du, G. Nayak, G. Oinuma, Z. Peng, and P. J. Bruggeman, "Effect of Water Vapor on Plasma Morphology, OH and H_2O_2 Production in He and Ar Atmospheric Pressure Dielectric Barrier Discharges," *Journal of Physics D: Applied Physics* 50 (2017): 145201.

37. A. Anders, "Glows, Arcs, Ohmic Discharges: An Electrode-Centered Review on Discharge Modes and the Transitions Between Them," *Applied Physics Reviews* 11 (2024): 031310.

38. P. Bruggeman, F. Iza, P. Guns, et al., "Electronic Quenching of OH(A) by Water in Atmospheric Pressure Plasmas and its Influence on the Gas Temperature Determination by OH(A-X) Emission," *Plasma Sources Science and Technology* 19 (2010): 015016.

39. W. Xi, H. Zhang, W. Ren, et al., "Mechanisms of OH and H_2O_2 Formation in the Liquid Phase Induced by an Atmospheric Pressure Plasma Jet with Oxygen Introduction," *Physics of Plasmas* 32 (2025): 083505.

40. P. Bruggeman and D. C. Schram, "On OH Production in Water Containing Atmospheric Pressure Plasmas," *Plasma Sources Science and Technology* 19 (2010): 045025.

41. T. K. Kim, T. Kim, I. Lee, K. Choi, and K. D. Zoh, "Removal of Tetramethylammonium Hydroxide (TMAH) in Semiconductor Wastewater Using the Nano-Ozone H2O2 Process," *Journal of Hazardous Materials* 409 (2021): 123759.

42. W. X. Chen, K. F. Chen, K. L. Chang, et al., "Photoelectrochemical Degradation of Tetramethylammonium Hydroxide by Green-Synthesized Ag-Modified Titanate Nanotube Arrays," *Journal of Environmental Chemical Engineering* 11 (2023): 110625.

43. M. Hori, "Radical-Controlled Plasma Processes," *Reviews of Modern Plasma Physics* 6 (2022): 36.

44. J. Lv, Y. Wang, M. Fu, C. Ou, and F. Xiao, "Removal of Tetramethylammonium Hydroxide (TMAH) from Thin-Film Transistor Liquid Crystal Display (TFT-LCD) Industry Wastewater by Hydrolysis Acidification-Aerobic and Anaerobic Processes," *Journal of Cleaner Production* 279 (2021): 123502.

45. V. V. Lobodin, P. Juyal, A. M. McKenna, R. P. Rodgers, and A. G. Marshall, "Tetramethylammonium Hydroxide as a Reagent for Complex Mixture Analysis by Negative Ion Electrospray Ionization Mass Spectrometry," *Analytical Chemistry* 85 (2013): 7803–7808.

46. R. Talviste, I. Jõgi, S. Raud, H. Noori, and J. Raud, "Nitrite and Nitrate Production by NO and NO2 Dissolution in Water Utilizing Plasma Jet Resembling Gas Flow Pattern," *Plasma Chemistry and Plasma Processing* 42 (2022): 1101–1114.

47. X. Fan, S. Kang, J. Li, and T. Zhu, "Formation of Nitrogen Oxides (N2O, NO, and NO2) in Typical Plasma and Plasma-Catalytic Processes for Air Pollution Control," *Water, Air, & Soil Pollution* 229 (2018): 351.

48. D. Xu, T. K. Srivastava, and P. J. Bruggeman, "Plasma-Induced Oxidation in Micro-Droplets: Quantifying H_2O_2 and OH Fluxes and Transport Limitations," *Plasma Chemistry and Plasma Processing* 45 (2025): 661–676.

49. D. Gan, L. Hong, S. Yuan, et al., "Energy-Efficient Production of Plasma-Activated Water: Insights Into Controllable Peroxynitrite Chemistry," *Green Chemistry* 27 (2025): 3715–3726.

Supporting Information

Additional supporting information can be found online in the Supporting Information section.
Supporting Information revised.